



CHORUS

This is the accepted manuscript made available via CHORUS. The article has been published as:

Microdomain dynamics in single-crystal BaTiO₃ during paraelectric-ferroelectric phase transition measured with time-of-flight neutron scattering

A. Pramanick, X. P. Wang, C. Hoffmann, S. O. Diallo, M. R. V. Jørgensen, and X.-L. Wang

Phys. Rev. B **92**, 174103 — Published 6 November 2015

DOI: [10.1103/PhysRevB.92.174103](https://doi.org/10.1103/PhysRevB.92.174103)

Microdomain dynamics in single-crystal BaTiO₃ during paraelectric-ferroelectric phase transition measured with time-of-flight neutron scattering

A. Pramanick,^{1,a} X. P. Wang,² C. Hoffmann,² S. O. Diallo,² M. R. V. Jørgensen,³ X.-L. Wang¹

¹ Department of Physics and Materials Science, City University of Hong Kong, Kowloon, Hong Kong SAR

² Chemical and Engineering Materials Division, Oak Ridge National Laboratory, Oak Ridge, Tennessee 37831, United States of America

³ Center for Materials Crystallography, iNano & Department of Chemistry, Aarhus University, Aarhus, Denmark

^aEmail: abhijit.pramanick@gmail.com

Abstract

Microscopic polar clusters can play an important role in the phase transition of ferroelectric perovskite oxides such as BaTiO₃, which have shown coexistence of both displacive and order-disorder dynamics, although their topological and dynamical characteristics are yet to be clarified. Here, we report sharp increases in the widths and intensities of Bragg peaks from a BaTiO₃ single crystal, which are measured *in situ* during cooling/heating within a few degrees of its phase transition temperature T_C , using a neutron time-of-flight Laue technique. Most significantly a sharper and stronger increase in peak widths and peak intensities were found to occur during cooling than that during heating through T_C . A closer examination of the Bragg peaks revealed their elongated shapes in both the paraelectric and ferroelectric phases, the analysis of which indicated the presence of microdomains that have correlated $\langle 111 \rangle$ -type polarization vectors within the $\{110\}$ -type crystallographic planes. No significant increase in the average size of the microdomains (~ 10 nm) near T_C could be observed from diffraction measurements, which is also consistent with small changes in the relaxation times for motion of Ti ions measured with Quasi-elastic-neutron-scattering (QENS). The current observations do not indicate that the paraelectric-ferroelectric phase transition in BaTiO₃ is primarily caused by an increase in the size of the microscopic polar clusters or critical slowing down of Ti ionic motion. The sharp and strong increases in peak widths and peak intensities during cooling through T_C is explained as a result of microstrains that are developed at microdomain interfaces during paraelectric-ferroelectric phase transition.

I. INTRODUCTION

Phase transitions are an important area of study in materials science, since they have significant implications for both processing of materials and their functionalities. For many phase transitions in crystalline solids, there occur only small changes in atomic positions or reorientations of molecular units, without a dramatic reconstruction of the crystal lattice. These kinds of structural phase transitions can be categorized into either (a) a displacive type, in which the order parameter for static atomic displacements undergo a change at the phase transition temperature, or (b) an order-disorder type, in which the order parameter is an average of several equivalent atomic displacements and some of them are biased across the phase transition point, thereby effecting a change in the average crystal structure [1,2].

In this context, the case of paraelectric-ferroelectric phase transition is quite fascinating, since it exemplifies that the displacive and order-disorder type mechanisms may not be exclusive and may co-exist for a material [2]. For example, the paraelectric-ferroelectric phase transition in prototype BaTiO_3 had been traditionally described as belonging to the displacive type, in which the equilibrium position of the Ti ion shifts off-center due to a freezing of the ferroelectric soft mode below the phase-transition temperature T_C [3]. However, subsequent investigations overwhelmingly demonstrated that the paraelectric-ferroelectric phase transition in BaTiO_3 also exhibits characteristics of an order-disorder type transition. For example, from measurements of dielectric susceptibility spectra in the paraelectric phase, broad peaks in the range of $10^8 - 10^{12}$ Hz were observed, which could be associated with different relaxation mechanisms such as coherent atomic motion in polar clusters, incoherent flipping of linearly correlated atomic chains and rustling interactions between neighboring atoms [4-7]. These measurements were further substantiated by observations of anomalous increases in optical index of refraction in the paraelectric phase [8], quasi-elastic neutron scattering that showed polarization fluctuations with relaxation time of $\tau \sim 5 \times 10^{-11}$ s [9], Brillouin light scattering that showed a Central Peak (CP) behavior arising from atomic relaxations in the 400-600 GHz range [10,11], Hyper-Raman measurements that showed a continuous decrease in mode frequency in the THz range [12] and X-ray speckle intensities that

indicated growth of fluctuating polar clusters of dimensions $< 1 \mu\text{m}$ upon approaching T_C from above [13,14]. Interestingly, relaxation modes were also observed for the paraelectric phase of BaTiO_3 in the slower 10^6 Hz range by photon correlation spectroscopy [15] and in the kHz range by NMR spectroscopy [16,17]. Some of these relaxation modes exhibited a certain degree of slowing down as the phase transition temperature T_C is approached from above, which supported the viewpoint of an order-disorder type transition in BaTiO_3 involving precursor polar clusters. In addition, a majority of these studies also concurred that the relaxing precursor clusters in the paraelectric phase should be associated with a dynamic off-centering of the Ti ions, although opinions differ on whether the Ti displacements are along the $\langle 001 \rangle$ or $\langle 111 \rangle$ directions in the paraelectric phase [17,18].

While the precursor polar clusters in the paraelectric phase were proposed to play an important role for the paraelectric-to-ferroelectric phase transition in classical ferroelectrics such as BaTiO_3 , their topology and governing dynamics close to T_C has notably remained unclear. A broad range of measured relaxation frequencies in the paraelectric phase makes this issue even more complicated, since it could indicate a broad size distribution for the precursor polar clusters. Due to a lack of clarity in this area, the microscopic mechanism for paraelectric-ferroelectric phase transition in even well known ferroelectrics, such as BaTiO_3 and KNbO_3 , is yet to be fully understood. Aside from its significance as a fundamental question in materials physics, the microscopic mechanism for paraelectric-ferroelectric phase transition is also of much practical importance, since it can help to explain and improve upon the performance of lead-free ferroelectric materials in several technological applications. Examples include losses in tunable capacitors [19] and long-term stability of electrocaloric and pyroelectric devices [20,21], for both of which the dynamics of precursor polar clusters are proposed to be instrumental.

Here, we used *in situ* neutron scattering experiments to investigate the characteristic changes in the shapes and dynamics of microscopic polar clusters in the ferroelectric compound of BaTiO_3 , as a function of temperature during cooling and heating through the paraelectric-ferroelectric phase transition temperature T_C . In order to characterize the extent of short-range spatial correlations within the

microscopic polar clusters, we analyzed the neutron Bragg diffraction peaks from BaTiO₃ single crystals. While the analysis of Bragg peak shapes is known to be an excellent tool for studying local atomic correlations in disordered relaxor ferroelectrics [22], the current measurements furthermore demonstrate the additional advantages of the neutron time-of-flight Laue technique, which allows for continuous monitoring of the scattered intensities without the need for any sample rotation. In addition to diffraction experiments, we undertook quasielastic neutron scattering (QENS) measurements from nanosized BaTiO₃ powders, in order to characterize the temporal nature of the atomic correlations within the microscopic polar clusters. The energy resolution of QENS allows for measurement of atomic dynamics in nanoseconds-to-picoseconds timescales for temperatures close to T_C. A comprehensive description of the microstructural dynamics during paraelectric-ferroelectric phase transition in prototypical BaTiO₃ is presented, while taking into account both diffuse neutron scattering and QENS measurements.

II. EXPERIMENTAL

Time-of-flight neutron diffraction measurements were taken from a 2 mm × 2 mm × 2 mm BaTiO₃ single crystal at the TOPAZ diffractometer of the Spallation Neutron Source (SNS). The crystal was originally obtained from MTI Corporation, CA, USA in the form of a rectangular sheet, which was then cut in the form of a cube and subsequently annealed at temperatures above the T_C prior to taking neutron diffraction measurements. The diffraction measurements were taken at TOPAZ, which is a neutron wavelength-resolved, or time-of-flight Laue diffractometer with an extensive area detector coverage capable of three-dimensional Q -space mapping from a stationary single-crystal at pre-defined setting angles. In a time-of-flight diffractometer such as TOPAZ, the scattering intensities from the crystal appear at the detector at different times-of-flight, which correspond to different wavelengths and therefore to different wavevectors \vec{Q} of momentum transfer. Consequently, in addition to resolving the scattered intensities in 2-dimensions that is afforded by the use of an area detector, further resolution for scattering intensities in the third dimension is obtained by recording the arrival times of the neutrons at the detector with respect to the beam pulse. In this manner, the 3-dimensional diffuse scattering patterns around the

Bragg peaks that arise due to short-range microscopic correlations could be obtained without the need for any rotation of the crystal during data collection.

In the first experiment, by taking advantage of the high neutron flux at TOPAZ and a unique timing methodology, we made a quick survey of the structural changes under dynamic/heating cooling conditions, which are often encountered in many practical applications. The crystal was cooled and heated continuously through T_C at a heating/cooling rate of 15 K/hour, and the scattered intensity was collected in situ in an uninterrupted manner during this process. Using an event-based data acquisition technique [23,24], the obtained dataset was rebinned into pseudo-constant-temperature slices by matching the particular time stamps associated with the neutron events and with the recorded temperatures. From this first experiment, we observed sharp changes in scattered intensities from the crystal close to its T_C , which also differed depending on whether the sample was cooled or heated through T_C . In order to investigate this phenomenon in detail, we subsequently made a detailed investigation of the Bragg peak shapes in a second experiment. For this second experiment, the crystal was positioned to monitor continuously the scattered intensities in different reciprocal lattice planes (r.l.p.), while the temperature was ramped up and down in steps of 1 K between 370 K and 435 K. At each temperature step, the sample was allowed to equilibrate for a period of 30 seconds, after which the neutron scattering pattern was collected for an additional 5 minutes. The Bragg peaks surveyed showed extended streaks of diffuse scattering, which were then analyzed with numerical calculations.

The QENS measurements were taken at the near-backscattering crystal-analyzer spectrometer BASIS of the SNS, over a temperature range similar to that of the diffraction experiments. The QENS measurements at BASIS provide an energy-resolution for measuring atomic dynamics in the ~ 1 ps to ~ 1 ns range [25,26]. The sample used for these measurements was in the form of nanocrystalline BaTiO_3 powder, which was placed inside a gap of 1 mm between two concentric cylindrical cans in order to minimize multiple scattering effects. Nanocrystalline powders ensured that uniformly scattered intensities with respect to the incident beam could be measured in all the detector banks, which were then summed

to get an adequate signal-to-noise ratio for detailed analysis of the energy-resolved dynamics in BaTiO₃. At each temperature, the QENS patterns were collected for a total time-period of 30 minutes.

III. RESULTS AND DISCUSSIONS

A. Changes in diffraction peak features during heating/cooling close to T_C

The contour plots in Figure 1(a) and 1(b) show the width of the integrated diffraction profiles around the (002) Bragg diffraction point as a function of temperature during continuous heating and cooling, respectively. In these plots, \vec{Q} is along the $[\bar{H}0H]$ direction within the (HOL) r.l.p. A single diffraction peak is observed in the cubic phase, which splits into two in the tetragonal phase. The T_C is determined from the temperature where the (002) Bragg diffraction peak splits. It can be noted that the behavior at the nominal phase transition temperature of T_C ~ 398 K are clearly different depending on whether the transition occurs from the tetragonal ferroelectric to the cubic paraelectric phase (heating), or in the reverse direction (cooling). We can also note a relatively large hysteresis of ~4 K for the transition temperature during heating and cooling, which betrays a first-order like character of the paraelectric-ferroelectric phase transition in BaTiO₃.

For quantitative analysis, the integrated peak intensities and the peak positions were obtained from Gaussian fits to the constant temperature slices in the diffraction data and are shown in Figures 1(c)-(d). The width of the peak Δq remains unchanged at most temperatures, and only increases sharply at T_C. Under cooling Δq increases by ~17% in a narrow interval on approaching T_C, while under heating Δq decreases by ~10 % on further heating above the T_C. In addition, a sharp increase in intensity can be observed close to T_C, which is larger during cooling than during heating. These features were also observed for other peaks over a broad area of the reciprocal space. In order to investigate the origins of such sharp changes in peak widths and peak intensities near T_C, a detailed survey of the different Bragg diffraction peaks were undertaken, the results from which are described below.

B. Analysis of the Bragg diffraction peaks

Figure 2 shows the 2-dimensional images of the $(1\bar{1}\bar{1})$ diffraction peak for temperatures 410 K and 400 K during cooling through T_C , as they appear in the (H,K,0), (H,0,L) and (0,K,L) reciprocal lattice planes (r.l.p.) when viewed along the [0,0,L], [0,K,0] and [H,0,0] directions, respectively. The scattered intensities for each image were integrated along direction normal to the respective r.l.p, that is, for example, for the image shown in the (H,K,0) r.l.p., the scattered intensities were integrated along the [0,0,L] direction. Moreover, the scattered intensities were also integrated over all energy transfers, which mean that we cannot discriminate between whether the structural disorders contributing to such diffuse scattering are static or represent temporally averaged states. For such discrimination, we present QENS measurements later in the article. The wavevector or q -resolutions at TOPAZ depends on the different detectors and were determined based on fitting of the diffraction patterns measured from a Si single crystal. For the detector that was used for measuring the $(1\bar{1}\bar{1})$ diffraction peak, $\Delta q/q$ is ~ 0.0038 . Most interestingly, we observe that there are diffuse streaks observed around the Bragg spots at both these temperatures beyond this resolution limit, and the characteristic shapes of the diffuse streaks stays more or less the same across T_C . The nominal value of $T_C \sim 403$ K during step-wise cooling was determined from the temperature below which the 1-D intensity profile of the $(00\bar{2})$ peak is split (see Figure S1 in Supplementary Information). At 410 K, the crystal is in the paraelectric phase as indicated by single peaks for the 1-D profiles of the $(00\bar{2})$ reflection. At 403 K, there is a splitting of the peak indicating the appearance of a non-centrosymmetric ferroelectric phase.

As can be seen from Figure 2(a), the $(1\bar{1}\bar{1})$ peak in the (H,K,0) r.l.p. has the appearance of a rod extended along the $[1\bar{1}0]$ direction and has a bulge in the middle. Similarly, in the (H,0,L) r.l.p. the diffuse streak is extended predominantly along $[10\bar{1}]$ direction and also has a bulge in the middle. However, the intensity distribution for the same peak appears as more circular or square-like in the (0,K,L) r.l.p., as compared to the extended shapes of the other two patterns described above. It is noteworthy that both in the (H,K,0) and (H,0,L) r.l.ps, the diffuse streaks are extended along directions

perpendicular to the respective wave-vectors of $[110]$ and $[101]$. For the (220) , $(\bar{2}20)$ and the $(00\bar{2})$ peaks, which are shown in Figures 2(b)-(d), similar features exist as described above, that is, the Bragg diffraction peaks are extended more or less transverse to the respective \vec{Q} vectors shown. Additional diffraction peaks are shown in Figure S2 in the Supplementary Information. The $\Delta q/q$ resolutions for these peaks were less than ~ 0.003 . Below we examine the origins of the elongated shapes of the Bragg peaks in BaTiO₃ single crystal close to T_C .

Diffuse scattering around Bragg points may arise due to the presence of defects or disorders that have short range correlations. For perfectly isotropic defects with spherical symmetry of displacements, the diffuse scattering intensity is proportional to $I_{diff} \propto [Q \cos \phi]^2 / q^2$ and is known as Huang scattering [27], where ϕ is the angle between the scattering wavevector \vec{Q} and the reduced wavevector \vec{q} near a Bragg point. For Huang scattering, the diffuse intensity is enhanced along \vec{Q} while it vanishes in case that \vec{q} is normal to \vec{Q} . An examination of the scattering patterns observed here reveals that this is not always satisfied, such as for reflection $(00\bar{2})$ shown in Figure 2(d). On the other hand, we note that anisotropic diffuse scattering patterns could also arise in ferroelectric materials as a result of planar short-range correlations of polarization vectors, such as shown earlier for nanoscale polar clusters in relaxor ferroelectrics [28,29]. Noting however that the current patterns shown in Figure 2 for BaTiO₃ are different from what was reported earlier for relaxors in Refs. [28,29], we examine below in detail the origins for the current observations.

We propose that the observed appearance of the elongated peak shapes in the different r.l.ps is a result of superposition of two types of plates at the respective Bragg peak positions. One set of these plates have their plane-normals parallel to $[1\bar{1}0]$ -type directions and are extended along $[001]$, as illustrated in Figure 2(e); consequently, they appear as extended rods in the $(H,K,0)$ r.l.p., but instead appear as rectangles in the $(H,0,L)$ and $(0,K,L)$ r.l.ps. Similarly, the other set of these plates have their

plane-normals parallel to $[10\bar{1}]$ -type directions and are extended along $[010]$; consequently, they appear as extended rods in the (H,0,L) r.l.p., but instead appear as rectangles in the (H,K,0) and (0,K,L) r.l.ps. The different kinds of possible planar correlations and consequent diffuse scattering patterns are illustrated in Figure 2(e). Note that when there is a superposition of a rod-like shape parallel to a $\langle 1\bar{1}0 \rangle$ -type direction and a rectangular shape parallel to a $\langle 100 \rangle$ -type direction, the overall peak appears like a rod with a bulge in the middle, such as can be seen in the top panel of Figure 2(a). On the other hand, when there is a superposition of two rectangles parallel to two $\langle 100 \rangle$ -type directions, such as in the bottom panel of Figure 2(a), the overall shape appears round- or square-like.

For the type of peak shape feature shown as A in Figure 2(e), such regions with short-range correlations should resemble narrow lamella bounded by walls that are parallel to $(1\bar{1}0)$ planes and are extended along $[001]$. Similarly, for the type of peak shape feature shown as B in Figure 2(e), the short-range correlations should resemble narrow lamella bounded by walls that are parallel to (101) planes and are extended along $[010]$. In support of this idea, we note that arrays of microdomains having dynamic characters and with domain-walls parallel to $\{011\}$ -type planes were indeed observed earlier with TEM in BaTiO_3 crystals for temperatures close to T_C in the ferroelectric phase [30]. Since, the shape of Bragg diffraction peaks observed here show close resemblance in both the ferroelectric and the paraelectric phases, we propose that both their origins lie in similar such arrays of microdomains in the material. It is conceivable that these microdomains constitute the relaxing precursor clusters in the paraelectric phase of BaTiO_3 that were proposed earlier, as described in the Introduction.

Next, we examine the directional nature of the short-range correlated polar vectors $\vec{\epsilon}$ within the proposed microdomains, while noting that diffuse scattering intensities from polar correlations are given by, $I \propto (\vec{Q} \cdot \vec{\epsilon})^2$ [31]. Let us consider the type of diffuse scattering observed for the (220) and $(00\bar{2})$

Bragg peaks in the (H,K,0) r.l.p. Note that both these peaks are elongated along the $[1\bar{1}0]$ direction, which indicates that diffuse scattering for the elongated peak shape should be due to short-range correlations within microdomain lamella parallel to the $(1\bar{1}0)$ planes. For the (220) peak, \vec{Q} is parallel to $[220]$, and therefore the correlated polar vectors $\vec{\epsilon}$ must have components along $[110]$ within the $(1\bar{1}0)$ planes for non-zero values of $\vec{Q} \cdot \vec{\epsilon}$. Similarly, for $(00\bar{2})$, peak \vec{Q} is parallel to $[00\bar{2}]$, and so, the correlated polar vectors $\vec{\epsilon}$ must have components along $[001]$ within the $(1\bar{1}0)$ planes for non-zero $\vec{Q} \cdot \vec{\epsilon}$. Therefore, in order to satisfy the condition that the correlated polar vectors $\vec{\epsilon}$ have components along both the $[110]$ and $[001]$ directions within the same $(1\bar{1}0)$ planes, we should consider that the polar vectors overall are oriented along $[111]$ -type directions. This is exactly the same direction along which the Ti atoms are displaced locally from the center of the unit cells in all the paraelectric and ferroelectric phases of BaTiO₃ [18].

Following the above arguments, we simulate the diffuse scattering profiles based on a model of lamellar microdomains within the crystal. Here we assume a cubic $Pm\bar{3}m$ space group for the BaTiO₃ unit cell, which contains only one Ti atom that is displaced from the unit cell center by vector $\vec{\epsilon}$ along a $[111]$ -type direction. The resultant polarizations are considered to be correlated within lamellar microdomains, such as observed earlier with TEM [30]. We further assume that the correlation for the polarization vectors within the microdomains decay exponentially, both in- and out-of-plane. In that case, for small Ti displacements, the diffuse scattering intensity can be modeled using the following equation [28,32]:

$$I_{diff}(\vec{Q}) = A \cdot b_{Ti}^2 \sum_i |\vec{Q} \cdot \vec{\epsilon}|^2 \frac{\Gamma_{\parallel}}{q_{\parallel i}^2 + \Gamma_{\parallel}^2} \cdot \frac{\Gamma_{\perp}}{q_{\perp i}^2 + \Gamma_{\perp}^2} \quad (1)$$

where A is a constant, b_{Ti} is the neutron scattering form factor for Ti; Γ_{\parallel} and Γ_{\perp} are the inverse of the correlation lengths for the polarization vector in- and out-of-plane, respectively; $q_{\parallel i}$ and $q_{\perp i}$ are the in- and out-of-plane components of the reduced wavevector \vec{q} near a Bragg point. We simulated the diffuse scattering patterns near the different Bragg points using Eq. (1) and a distribution of lamellar domains such as shown in Figure 2(d), which have dimensions between 4-10 nm. The calculations were performed using the commercial package IGORPro. The simulated patterns are shown adjacent to the respective experimental measurements in Figure 2. In general, the simulated patterns closely resemble the measured patterns in terms of their general orientations and widths in reciprocal space. Here, a closer look at the (220) and $(\bar{2}20)$ Bragg peaks in the (H,K,0) r.l.p, which are shown in Figure 2(b) and (c), is particularly interesting as they clearly reveal the different orientation of the diffuse scattering patterns at these two points. The (220) peak is extended primarily along $[1\bar{1}0]$ direction, while the $(\bar{2}20)$ peak is extended primarily along $[110]$. In the first case, \vec{Q} is parallel to $[220]$, and therefore diffuse scattering is only observed for \vec{E} that have components along $[110]$ within the $(1\bar{1}0)$ planes. In the second case, \vec{Q} is parallel to $[\bar{2}20]$, and therefore diffuse scattering is only observed for \vec{E} that have components along $[\bar{1}10]$ within the (110) planes. Some minor differences between the simulated and the measured patterns could be due to more complex domain structures that were not considered here or due to the presence of microstrains whose contributions are further described in Section C.

C. Temperature-dependent changes in Bragg peak shapes near T_C

The appearance of the $(1\bar{1}\bar{1})$ Bragg peaks at 1 K temperature intervals near T_C are shown in Figure 3(a), which were collected during both heating and cooling. As can be seen from Figure 3(a), the transverse width of the extended rod-shaped $(1\bar{1}\bar{1})$ peak (marked by the red line) increases abruptly during cooling at temperatures 404 K and 403 K, below which the peak width abruptly decreases again.

Within the same temperature range, a similar behavior is observed for the integrated peak intensity, where it increases abruptly to its maximum value at 403 K. Similar trends for the transverse widths and integrated intensities of the $(1\bar{1}\bar{1})$ peak shape were also observed when plotted in the (H,K,0) r.l.p (not shown in 2-D plots). Notably, the trends are characteristically different during heating, during which we observe a more gradual change in peak widths and intensities with temperature.

In order to describe the observed trends quantitatively, the peak intensity profiles were fit to a Gaussian peak profile function, the results of which are shown in Figure 3(b)-(c). In Figures 4(b), Δq represents the full-width-at-half-maximum (FWHM) of the peaks in terms of the wavevector \vec{q} , where \vec{q} is oriented approximately either along along $[101]$ direction (in (H,0,L) r.l.p.). The value for Δq remains unchanged for most temperatures below and above T_C , indicating that the average dimensions of the microdomains (d) do not change. The dimensions of the microdomains (~ 10 nm) obtained above is only an estimate, since the broadening of the diffraction peaks is partly also due to microstrains, which we further discuss below. In absolute numbers, our results from diffraction peak width measurements are close to those reported earlier from TEM measurements (25-100 nm) [30] and PCS experiments (~ 200 nm) [15], while they are lower than the width of polar clusters reported from X-ray speckle scattering and optical birefringence measurements ($\sim 1 \mu\text{m}$) [13,11]. Note that the spatial correlation lengths obtained from neutron diffraction peak widths represent the temporally averaged states of the microdomains, while measurements such as speckle scattering and PCS provide information on the transient states of photocreated polar clusters over timescales ranging from picoseconds to microseconds. Also, the current measurements are from the bulk of the material volume, while speckle measurements using soft X-rays were surface sensitive. Nevertheless, in spite of these differences regarding the details of each specific measurement technique, they all tend to indicate that there is no significant increase in the size of polar clusters with temperatures upon approaching T_C . In light of these findings, the theoretical assertion that the precursor polar domains grow upon approaching T_C needs to be further reevaluated [33].

The outstanding question remains why is there an abrupt increase in the diffraction peak width and intensity at T_C during cooling (Figure 3(b)-(c))? One possible contribution to the increased peak intensity as T_C is approached could be from increased polarization fluctuations within the microscopic domains, as shown earlier in Ref. 13, however it does not explain the abrupt increase in diffraction peak widths. The increase in the transverse width of the diffraction peaks, such as seen from Figures 3(b), can be caused by both due to decrease in microdomain widths as well as due to an increase in microstrains. We used the modified Williamson-Hall method to distinguish between the two [34]. In this approach, Δd or the lattice d -spacing span around the mean \bar{d} of a particular diffraction peak is plotted with respect to the actual d -spacing of an hkl lattice plane, and then the slope of the line is proportional to the magnitude of microstrains $\epsilon = \Delta d / d$ in the material. The plots are shown in Figure 4(a) and 4(b), for the measurements of peak widths in the (H,K,0) and the (H,0,L) r.l.p.s, respectively. The lattice d -spacing spans obtained from experimental observations Δd_{obs} are plotted after taking into account the instrumental broadening for the different detectors of TOPAZ Δd_{ins} . The slopes of the linear fits indicate microstrains of $\epsilon \sim 1\%$, which is of the same order as the ferroelectric lattice distortion in BaTiO₃. There is a clear increase in the slope while cooling from 408 K to 403 K, which indicates that the microstrains in the crystal is increased by 25%-40% as the T_C is approached within a few degrees, and is the primary cause for abrupt broadening of transverse widths of the diffraction peaks. It can be noted that previous measurements with X-ray speckle scattering has shown that upon approaching T_C from above, while the size of the microscopic polar clusters remain same, the distance between them decreases and eventually approaches their exact dimensions [13]. This indicates in effect an increase in microdomains population, which should consequently lead to an increase in the interfacial area between the microdomains and also will lead to the development of microstrains at interfaces - both of these factors can cause increases in diffraction peak width and scattering intensities (due to extinction effects), such as can be observed in Figure 3. Upon crossing the phase transition point, the microdomains are likely

rearranged that is allowed by changes in material dimensions, which leads to a subsequent minimization of the interfacial microstrains.

During heating, the situation is different since there are no new additions to the microdomain population in going from the ferroelectric to the paraelectric phase, and therefore the microstrains resulting during phase transition can be more easily relaxed. This is likely the reason why we observe a less abrupt fluctuation in peak width and intensity near T_C for the ferroelectric-to-paraelectric phase transition during heating. The current results regarding abrupt microstructural changes can be reconciled with strong acoustic emissions at the same temperatures observed from single crystals of BaTiO_3 during thermal cycling through T_C , which also showed that the acoustic emissions are stronger during cooling than that during heating [35].

D. Atomic dynamics within microdomains

The size of the polar clusters in the paraelectric and the ferroelectric phases of BaTiO_3 should ultimately depend on the underlying dynamics at the microscopic length scales. As introduced in the beginning of the article, the wide range of reported time periods for microscopic dynamics in BaTiO_3 near T_C indicates a concurrence of several relaxation mechanisms operating at different time scales. Therefore in order to understand the evolution of the microdomain characteristics across the paraelectric-ferroelectric phase transition temperature, a clarification of these different dynamics is in order.

The very fast dynamics at the high end of the frequency spectrum are dominated by resonance phenomena related to phonons or lattice vibrations, the timescales for which are typically less than a picosecond. For BaTiO_3 in this timescale range, interesting effects related to an overdamping of the soft optic phonon mode and interference between acoustic and optic modes near T_C have been reported earlier.^{9,36} However, since here our focus will be on the microscopic relaxation phenomena, which occur on timescales longer than that of phonons, we will not discuss these effects in detail.

Previous dielectric measurements in BaTiO₃ crystals also showed a Debye-like frequency response in the THz frequency range that is strongly temperature dependent. Close to T_C, the timeperiod for this Debye mode was shown to exhibit a slowing down to $\sim 20 \text{ cm}^{-1}$ (or $\sim 2 \text{ ps}$) [6]. This was further substantiated by the presence of a temperature-dependent relaxation-type Central Mode (CM) from light scattering measurements that showed a characteristic Lorentzian spectral response in range of $\sim 1\text{-}4 \text{ ps}$ near T_C [11,37]. The origin of this particular relaxation mode was tentatively attributed to a tunneling or hopping motion of Ti ions between the several disordered sites that have local potential minima based on the order-disorder model of Comes et al. [18]; some of these minima are in a privileged (or ground) state while others are in an excited state, depending on local dipolar interactions. However, these earlier measurements of atomic dynamics by Brillouin light scattering experiments could be influenced by surface effects, and therefore an independent measurement of this relaxation mode with a bulk measurement technique is desirable.

Here, we used Quasi-Elastic-Neutron Scattering (QENS) from nanosized BaTiO₃ powders for the purpose of probing the dynamics of atomic tunneling near T_C. QENS enables characterization of ionic motion in bulk solids for time periods in the range of $10^{-9} - 10^{-12} \text{ s}$ (*ns to ps*) [25], which matches with the typical timescales of dynamic ionic motion in perovskite oxides. Moreover, since the different ionic species have different incoherent neutron scattering cross-sections, we can selectively probe the dynamics of one kind of ions in a material using this technique. Since, the incoherent neutron scattering cross-section of Ti (2.87 barns) is much more than that of O (0.0008 barns) and Ba (0.15 barns), the measured QENS spectra from BaTiO₃ can be primarily attributed to that originating from the dynamics of Ti motion [38].

Figure 5(a) shows the temperature dependence of the normalized Elastic Incoherent Neutron Scattering (EINS) $I(T)/I(T_0)$, where $I(T_0)$ refers to the scattering intensity measured at the lowest investigated temperature of 100 K. EINS is due to the scattering structure factor $S_{inc}(Q, \omega \approx 0)$, which corresponds to the elastic Debye-Waller vibrations in a narrow energy range close to $\omega \approx 0$. With

increasing temperature, the EINS decreases, more or less linearly, as the higher energy vibrational states get increasingly populated. It could be noticed that beyond 300 K, the EINS signal becomes increasingly noisy, which could be due to thermal fluctuations during equilibration.

In order to make a detailed analysis of the prevalent dynamics for temperatures 300 K and above, the quasielastic (QE) spectra were collected at selected temperatures with longer counting times. The results are shown in Figure 5(b). For each temperature, the scattering patterns from all Q values were folded into a single spectrum and the resultant spectrum was fitted with a Lorentzian peak profile function. The half-width-at-half-maximum (HWHM) Γ of each spectrum is then used to calculate the temperature dependent relaxation time τ , using the relation $\tau = (\hbar/\Gamma)$, the results of which are shown in Figure 5(c). In the paraelectric phase, $\tau \sim 7.5$ ps at 450 K, whereas in the ferroelectric tetragonal phase, $\tau \sim 12.5$ ps at 375 K. In general, τ increases with decreasing temperature and the temperature dependence could be fitted with an exponential relation $\tau \propto \exp(-E_A/kT)$, where E_A is the energy barrier for the particular type of motion, k is Boltzmann constant and T is absolute temperature. By fitting the temperature-dependent data, we obtained $E_A \sim 9.8$ kJ/mol or 0.1 eV/formula unit. The current measurements of τ closely matches with that obtained earlier from Brillouin light scattering experiments. Furthermore, the current estimate of the energy barrier of $E_A \sim 0.1$ eV is also consistent with that obtained by Sokoloff et al. [37], although they used a more complicated model for tunneling of ions. In addition, based on ion-specific neutron scattering cross sections, we can distinguish here between the different ionic species and uniquely identify that the observed dynamics from QENS measurements is due to a hopping or tunneling motion of Ti ions in the material, which exhibits an exponential behavior with temperature. Our measurements are somewhat different from that by Namikawa *et al.* who reported a slowing down of dynamics from ~ 20 ps to ~ 90 ps at 4.5 K above T_C [14], although we can note that even there the relaxation times did not truly diverge.

Finally, in addition to phonon vibrations and atomic tunneling motion at shorter time scales, relaxation mechanisms were also reported for BaTiO₃ in the range of several microseconds using photon

correlation spectroscopy [15]. These dynamics are likely due to the collective flipping of dipoles within microscopic polar regions, which should be slower than the kind of tunneling motion described above. However, since the collective flipping of the dipoles ultimately occurs as a result of hopping of the individual Ti ions, the rate of Ti hopping motion should be an important influential factor for the average size of the metastable polar clusters. Therefore, the observation that the microdomain sizes more or less remain constant across T_C is consistent with the fact that τ for Ti hopping motion does not change significantly near T_C . In other words, contrary to what is otherwise conceived, the current results do not indicate that the paraelectric-ferroelectric phase transition in BaTiO_3 is a primary result of growth in size of microscopic polar clusters or extreme slowing down of the tunneling motion of Ti ions near T_C .

IV. CONCLUSIONS

The following are the primary conclusions drawn here from neutron scattering experiments regarding the microscopic changes near paraelectric-to-ferroelectric transition in the prototypical perovskite ferroelectric BaTiO_3 :

- (A) Elongated shapes of Bragg diffraction peaks were observed from BaTiO_3 single crystal using time-of-flight neutron diffraction, whose average characteristics remained unchanged while going from the paraelectric to the ferroelectric phase and vice-versa
- (B) Analysis of the Bragg peaks indicated that the likely origin of the elongated shapes of the peaks is due to existing polar microdomains, which have polar vectors oriented along $\langle 111 \rangle$ -type directions and are correlated within $\{110\}$ -type planes.
- (C) The average size of the microdomains (~ 50 nm) remains approximately constant at all measured temperatures near T_C , which is also consistent with small changes in relaxation times τ for hopping motion of Ti ions in the material
- (D) Sharp increases in diffraction peak widths and peak intensities are observed for temperatures within a few degrees of T_C , which can be explained as a result of developing microstrains at

interfaces between the microdomains. These features are observed to be stronger during cooling than during heating.

In general, it is demonstrated that by combining Laue neutron diffraction and quasi-elastic neutron scattering measurements at a time-of-flight source, the temperature-dependent mesoscopic mechanisms during phase transitions in ferroelectric perovskite oxides can be analyzed very effectively, both under quasistatic and dynamic heating/cooling conditions. Therefore, the future applications of these techniques can be particularly helpful for the development of new lead-free ferroelectrics in which the phase transition mechanisms at mesoscopic length scales are yet to be fully determined [39].

ACKNOWLEDGEMENTS

The neutron scattering measurements were carried out at the Spallation Neutron Source, which is sponsored by the Division of Scientific User Facilities, Office of Basic Energy Sciences, US Department of Energy, under contract DE-AC05-00OR22725 with UT-Battelle, LLC. AP greatly acknowledges funding support from City University of Hong Kong. MRVJ is grateful for the support by the Danish National Research Foundation (DNRF93) and Danish Research Council for Nature and Universe (Danscatt). AP and XLW gratefully acknowledges funding support by a grant from the Research Grants Council of Hong Kong Special Administrative Region (Project No. CityU 122713). Technical assistance from Matthew Frost and Junhong Helen He is gratefully acknowledged.

References:

- [1] C. Kittel, Introduction to Solid State Physics (John Wiley & Sons, Inc, 2005).
- [2] M. E. Lines and A. M. Glass, Principles and Applications of Ferroelectrics and Related Materials (Clarendon Press, Oxford, 1977).
- [3] W. Cochran, Adv. Phys. **9**, 387 (1960).
- [4] M. Maglione, R. Böhmer, A. Loidl and U. T. Höchli, Phys. Rev. B **40**, 11441 (1989).
- [5] I. Ponomareva, L. Bellaiche, T. Ostapchuk, J. Hlinka and J. Petzelt, Phys. Rev. B **77**, 012102 (2008).
- [6] J. Hlinka, T. Ostapchuk, D. Nuzhnyy, J. Petzelt, P. Kuzel, C. Kadlec, P. Vanek, I. Ponomareva and L. Bellaiche, Phys. Rev. Lett. **101**, 167402 (2008).
- [7] H.-Y. Deng, Eur. Phys. Lett. **100**, 27001 (2012).
- [8] G. Burns and F. H. Dacol, Solid State Comm. **42**, 9 (1982).
- [9] Y. Yamada, G. Shirane and A. Linz, Phys. Rev. **177**, 177 (1969).
- [10] J.-H. Ko, S. Kojima, T.-Y. Koo, J. H. Jung, C. J. Won and N. J. Hur, Appl. Phys. Lett. **93**, 102905 (2008).
- [11] J.-H. Ko, T. H. Kim, K. Roleder, D. Rytz and S. Kojima, Phys. Rev. B **84**, 094123 (2011).
- [12] H. Vogt, J. A. Sanjurjo and G. Rossbroich, Phys. Rev. B **26**, 5904 (1982).
- [13] R. Z. Tai, K. Namikawa, A. Sawada, M. Kishimoto, M. Tanaka, P. Lu, K. Nagashima, H. Maruyama and M. Ando, Phys. Rev. Lett. **93**, 087601 (2004).
- [14] K. Namikawa, M. Kishimoto, K. Nasu, E. Matsushita, R. Z. Tai, K. Sukegawa, H. Yamatani, H. Hasegawa, M. Nishikino, M. Tanaka and K. Nagashima, Phys. Rev. Lett. **103**, 197401 (2009).

- [15] R. Yan, Z. Guo, R. Tai, H. Xu, X. Zhao, D. Lin, X. Li and H. Luo, *Appl. Phys. Lett.* **93**, 192908 (2008).
- [16] B. Zalar, V. V. Laguta and R. Blinc, *Phys. Rev. Lett.* **90**, 037601 (2003).
- [17] B. Zalar, A. Lebar, J. Seliger, R. Blinc, V. V. Laguta and M. Itoh, *Phys. Rev. B* **71**, 064107 (2005).
- [18] R. Comes, M. Lamber and A. Guinier, *Solid State Comm.* **6**, 715 (1968).
- [19] L. M. Garten, P. Lam, D. Harris, J.-P. Maria S. Trolier-McKinstry, *J. Appl. Phys.* **116**, 044104 (2015).
- [20] S. Pamir Alpay, J. Mantese, S. Trolier-McKinstry, A. Zhang and R. G. Whatmore, *MRS Bulletin* **39**, 1099 (2014).
- [21] X. Moya, S. Kar-Narayan and N. D. Mathur, *Nat. Mater.* **13**, 439 (2014).
- [22] G. Xu, P. M. Gehring and G. Shirane, *Phys. Rev. B* **74**, 104110 (2006).
- [23] H. Nojiri, S. Yoshii, M. Yasui, K. Okada, M. Matsuda, J.-S. Jung, T. Kimura, L. Santodonato, G. E. Granroth, K. A. Ross, J. P. Carlo and B. D. Gaulin, *Phys. Rev. Lett.* **106**, 237202 (2011).
- [24] X.-L. Wang, K. An, L. Cai, Z. Feng, S. E. Nagler, C. Daniel, K. J. Rhodes, A. D. Stoica, H. D. Skorpenske, C. Liang, W. Zhang, J. Kim, Y. Qi and S. J. Harris, *Sci. Rep.* **2**, 747 (2012).
- [25] E. Mamontov and K. W. Herwig, *Rev. Sci. Instrum.* **82**, 085109 (2011).
- [26] Z. Xu, J. Wen, E. Mamontov, C. Stocks, P. M. Gehring and G. Xu, *Phys. Rev. B* **86**, 144106 (2012).
- [27] K. Huang, *Proc. R. Soc. A* **190**, 102 (1947)
- [28] G. Xu, Z. Zhong, H. Hiraka and G. Shirane, *Phys. Rev. B* **70**, 174109 (2004).
- [29] M. Paściak, M. Wolczyk and A. Pietraszko, *Phys. Rev. B* **76**, 014117 (2007).

- [30] L. A. Bursill and P. J. Lin, *Nature* **311**, 550 (1984).
- [31] H. You and Q. M. Zhang, *Phys. Rev. Lett.* **79**, 3950 (1997).
- [32] A. Cervellino, S. N. Gvasaliya, O. Zaharko, B. Roessli, G. M. Rotaru, R. A. Cowley, S. G. Lushnikov, T. A. Shaplygina, M. T. Fernandez-Diaz, *J. Appl. Cryst.* **44**, 603 (2011).
- [33] A. Bussmann-Holder, H. Beige and G. Völkel, *Phys. Rev. B* **79**, 184111 (2009).
- [34] Y. Zhao and J. Zhang, *J. Appl. Cryst.* **41**, 1095 (2008).
- [35] E. Dul'kin, J. Petzelt, S. Kamba, E. Mojaev and M. Roth, *Appl. Phys. Lett.* **97**, 032903 (2010).
- [36] J. Harada, J. D. Axe and G. Shirane, *Phys. Rev. B* **4**, 155 (1971).
- [37] J. P. Sokoloff, L. L. Chase and D. Rytz, *Phys. Rev. B* **38**, 597 (1988).
- [38] www.ncnr.nist.gov/resources/n-lengths/
- [39] V. V. Shvartsman, D. C. Lupascu, *J. Am. Ceram. Soc.* **95**, 1 (2012)

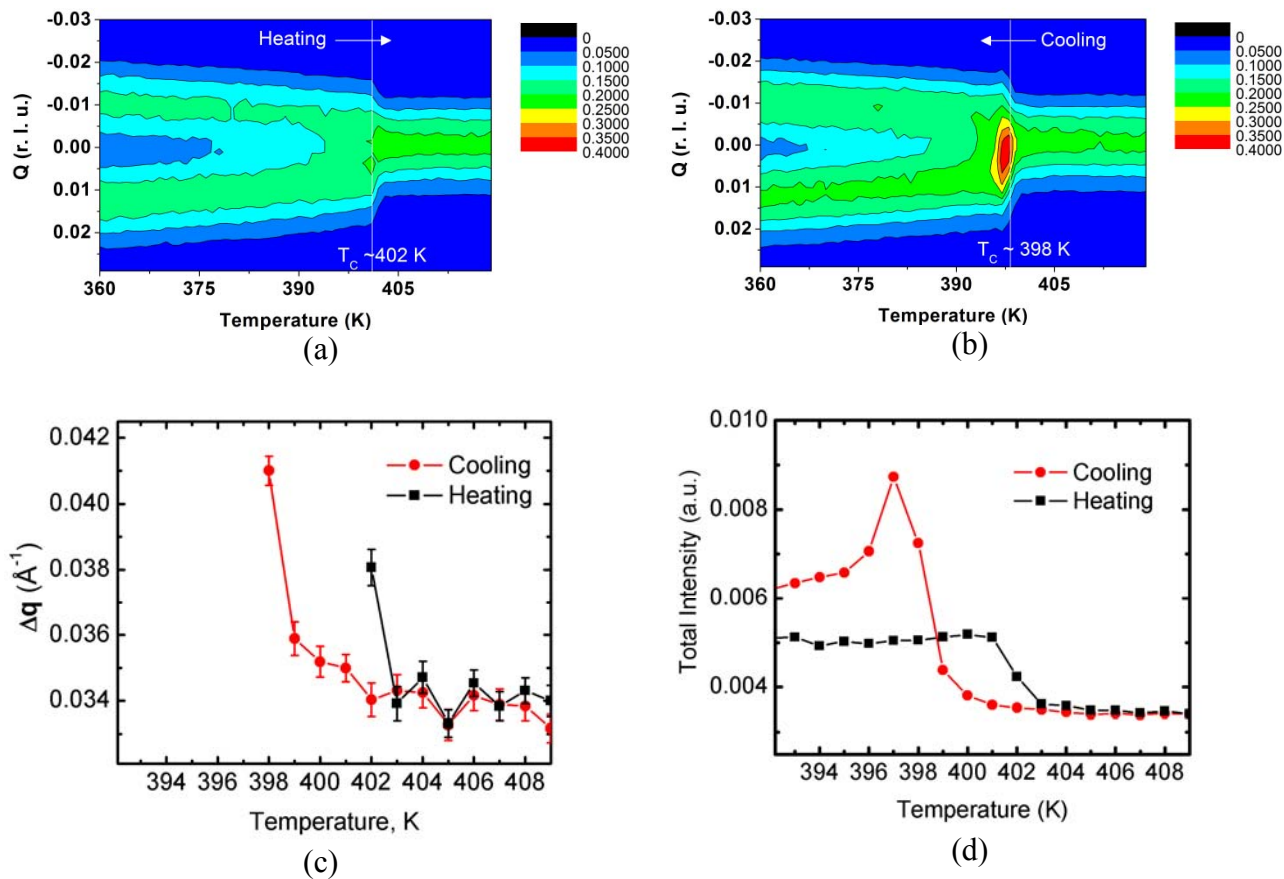
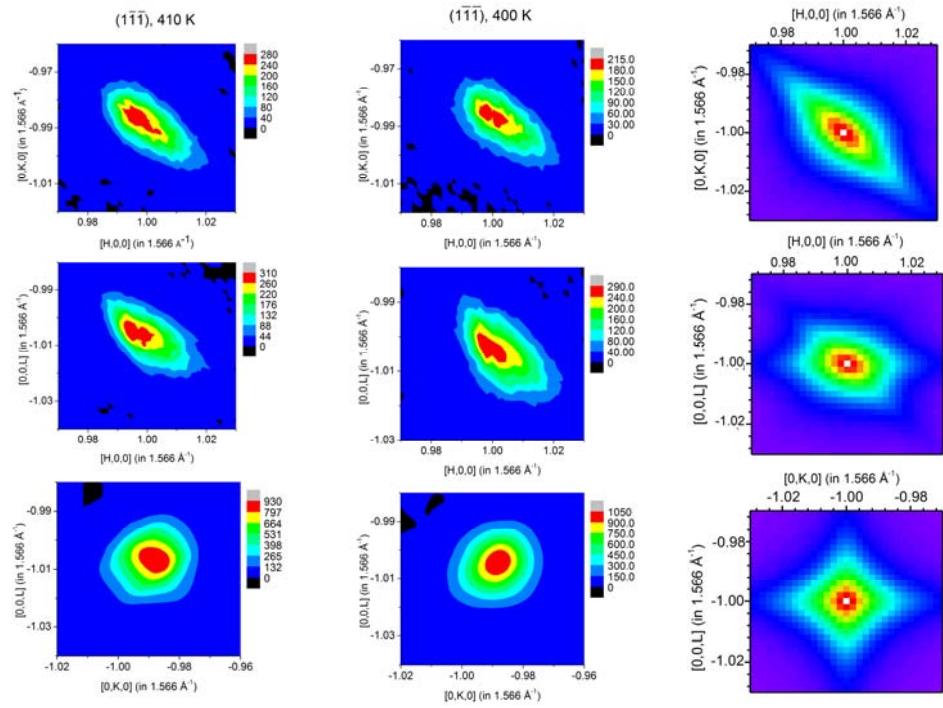
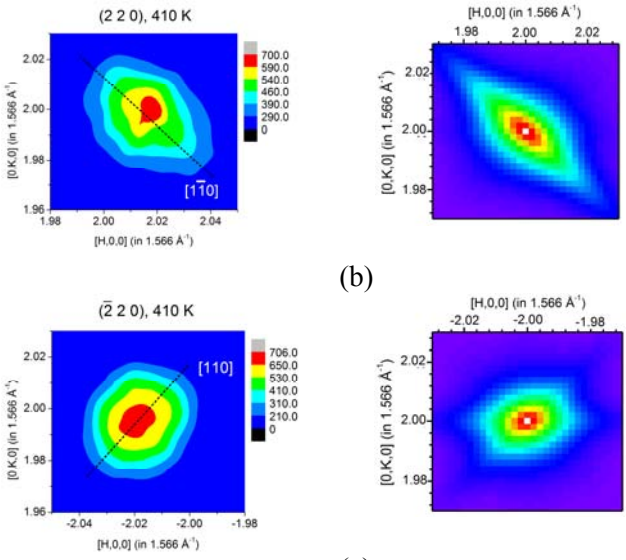


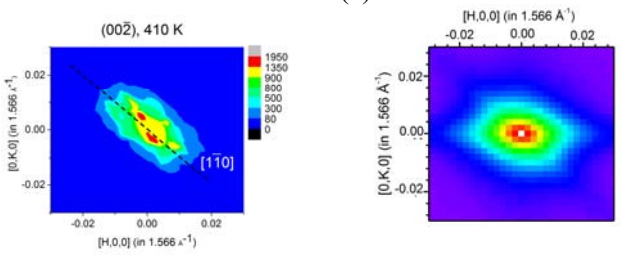
Figure 1: (a),(b) Contour plots showing width of the (002) diffraction peak in (H,0,L) r.l.p. during continuous heating and cooling through $T_C \sim 398$ K, respectively. (c),(d) show quantitatively the corresponding changes in peak width Δq and integrated intensity as a function of temperature.



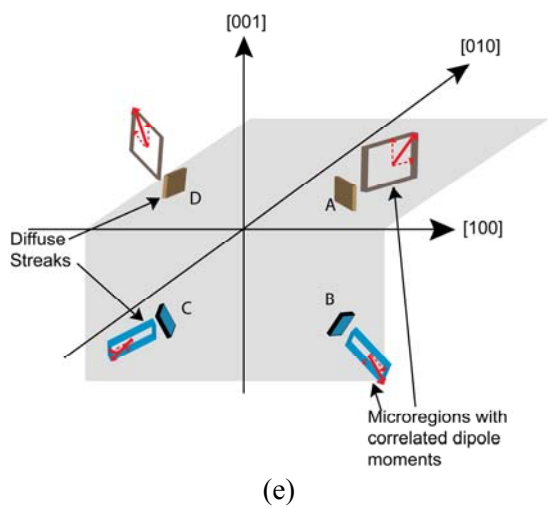
(a)



(b)



(d)



(e)

Figure 2: (a) The 2-D scattering intensity profiles of the $(1\bar{1}\bar{1})$ diffraction peak in the (H,K,0), (H,0,L) and (0,K,L) r.l.ps. at 410 K (paraelectric phase) and at 400 K (ferroelectric phase); (b,c,d) The 2-D scattering intensity profiles of the (220) , $(\bar{2}\bar{2}0)$ and $(00\bar{2})$ diffraction peaks in the (H,K,0) r.l.p. at 400 K. (e) A schematic of the proposed microdomains, which give rise to the diffuse streaks of the different Bragg diffraction peaks. The intensity scales for each plot are adjusted in accordance with the scattered intensity for each peak, which depends among other factors on the respective structural phases as well as the integration range for each pixel for different viewing angles. The simulated diffuse scattering patterns are shown adjacent to the corresponding measured patterns for each diffraction peak.

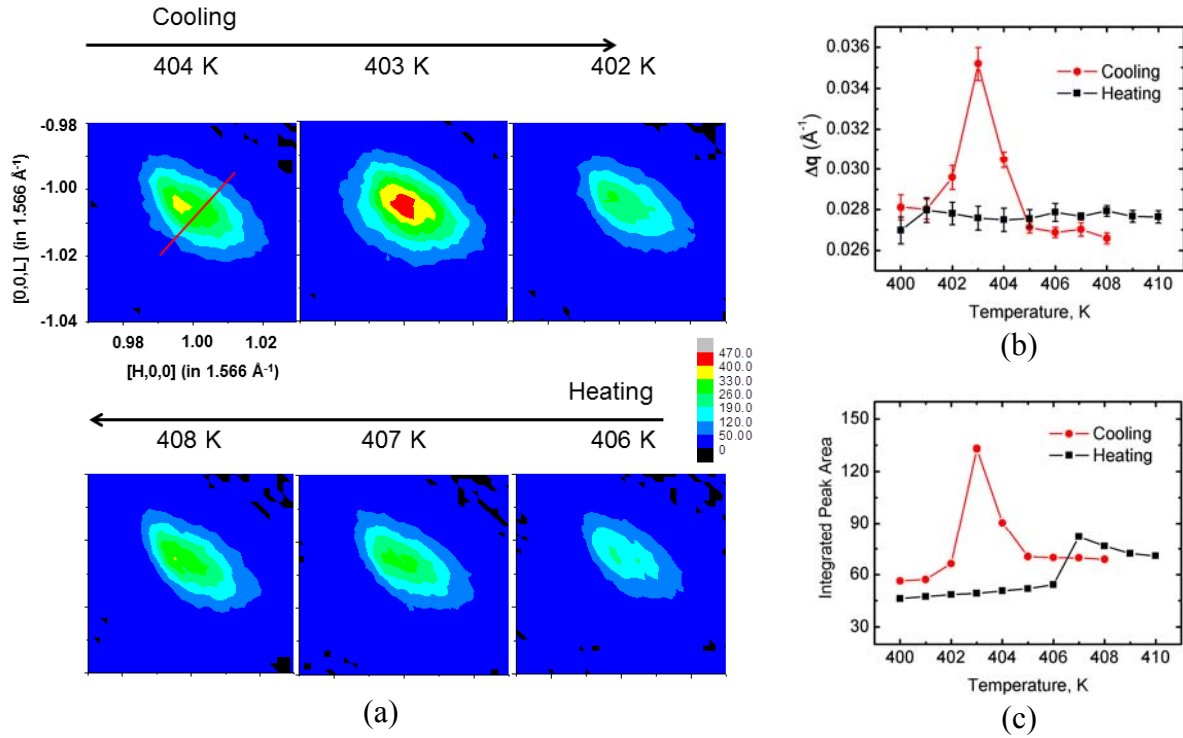
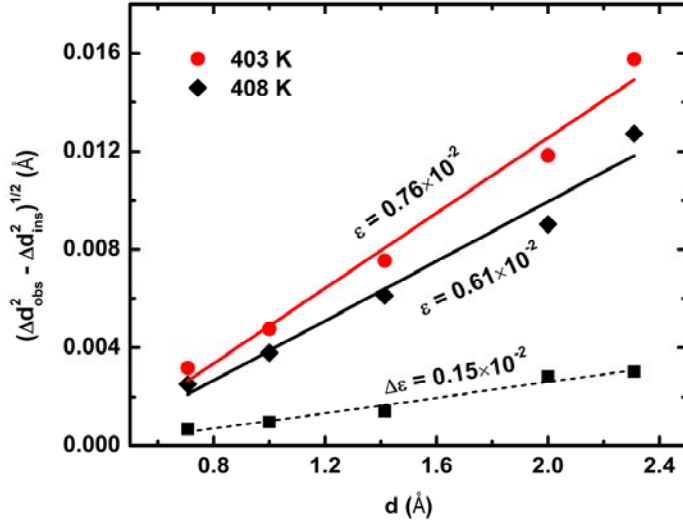
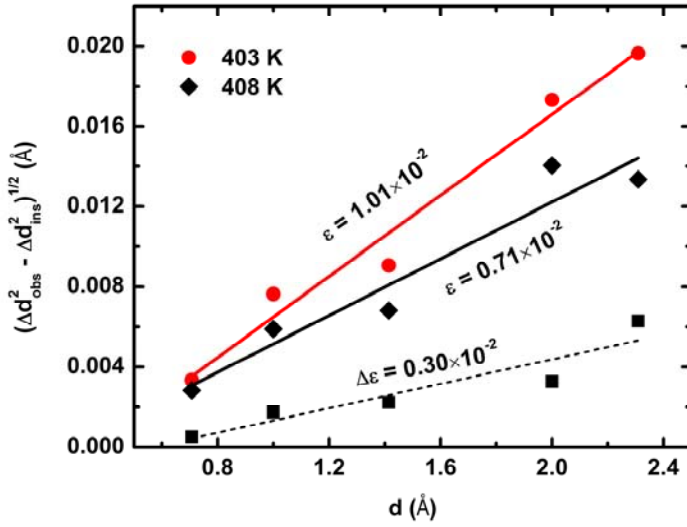


Figure 3: (a) The $(1\bar{1}\bar{1})$ diffraction peak at 1 K temperature intervals near T_C during cooling (above) and heating (below) through the paraelectric-ferroelectric phase transition. (b) The transverse widths Δq of the integrated 2-D intensity patterns (such as shown by the straight red line in (a)) as a function of temperature measured in the $(H,0,L)$ r.l.p.. (d) The integrated $(1\bar{1}\bar{1})$ peak intensities as a function of temperature.



(a)



(b)

Figure 4: Modified W-H plot of $(\Delta d_{obs}^2 - \Delta d_{ins}^2)^{1/2}$ for $(1 \bar{1} \bar{1})$ peak with respect to d for (a) (H,K,0) and (b) (H,0,L) r.l.p.s. The slopes of the solid lines from linear fits indicate the extents of microstrains within the crystal at 408 K and 403 K. The slope of the dashed line shows increase in microstrains $\Delta \epsilon$ upon cooling from 408 K to 403 K. The error bars for the data points are comparable to the plotted symbols.

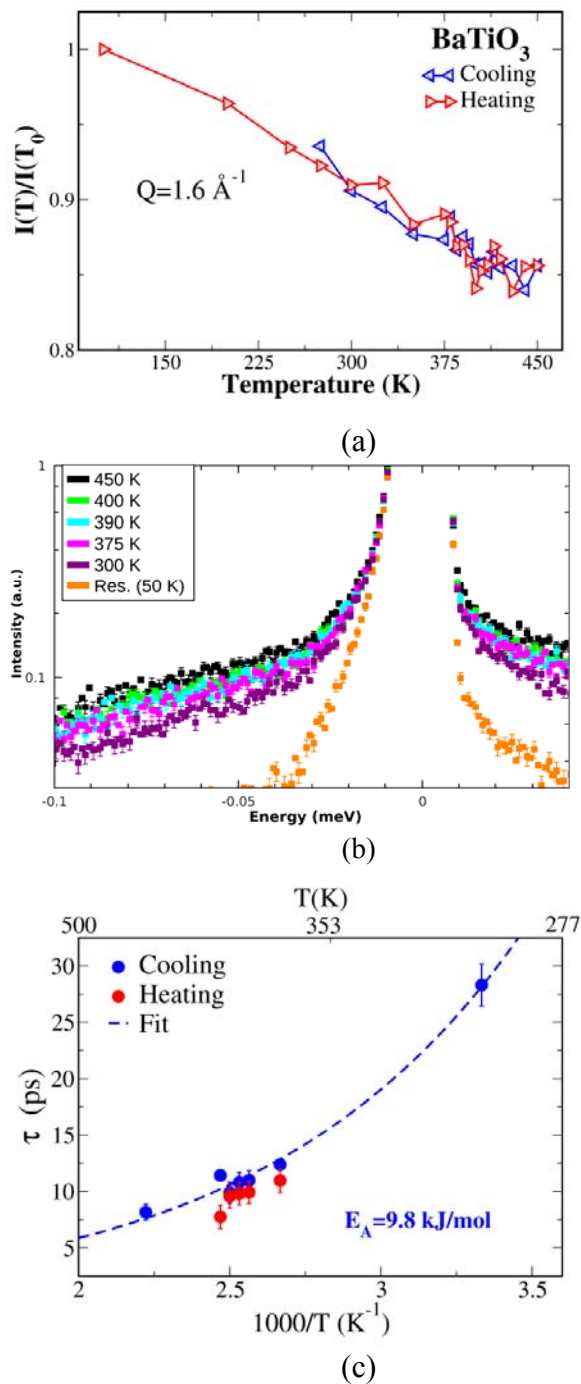


Figure 5: (a) The temperature dependence of the normalized Elastic Incoherent Neutron Scattering (EINS) $I(T)/I(T_0)$, where $I(T_0)$ refers to the scattering intensity measured at the lowest measured temperature of 100 K. (b) Quasi-elastic Neutron Scattering (QENS) spectra shown for selected temperatures. (c) Relaxation times τ obtained from fitting of the QENS spectra as a function of temperature; the temperature dependence of τ exhibits an Arrhenius behavior with an activation energy barrier of $E_A \sim 9.8 \text{ kJ/mol}$ or $0.1 \text{ eV/formula unit}$.